Next-nearest neighbour contributions to P $2p_{3/2}$ X-ray photoelectron binding energy shifts of mixed transition-metal phosphides $M_{1-x}M'_xP$ with the MnP-type structure

Andrew P. Grosvenor*, Ronald G. Cavell, Arthur Mar

Department of Chemistry, University of Alberta, Edmonton, Alberta, Canada T6G 2G2

Abstract

X-ray photoelectron (XPS) and X-ray absorption (XANES) spectroscopic measurements have been made for several series of mixed transition-metal phosphides $M_{1-x}M'_xP$ ($Co_{1-x}Mn_xP$, $Mn_{1-x}V_xP$, and $Co_{1-x}V_xP$), which adopt the MnP-type structure (M is more electronegative than M'). The P $2p$ binding energy shifts displayed by the mixed metal phosphide members do not follow the trend shown by the simple binary phosphides, a deviation which arises from the contribution of next-nearest neighbour effects operating on the primary photoemission site. The magnitude of this contribution can be derived from a simple charge potential model taking the metal electronegativity differences into account. It is suggested that these next-nearest neighbour contributions induce a charge transfer between the two dissimilar metals via metal–metal bonding, which modifies the Madelung potential experienced at the photoemission site. This charge transfer has been confirmed by analysis of the Co $2p$ XPS spectra as well as the P and Mn K-edge XANES spectra.
© 2007 Elsevier Inc. All rights reserved.

Keywords: XPS; Next-nearest neighbour shift; Plasmon loss; Transition-metal phosphides; XANES

1. Introduction

X-ray photoelectron spectroscopy (XPS) has been widely used to study the surfaces of materials (in particular, adsorbates and films). However, the application of XPS to bulk materials can also yield considerable insight into the properties and electronic structure of the constituent elements. In the case of intermetallic compounds, where the interpretation of binding energy (BE) shifts is more difficult, XPS has not been applied extensively. In general, variations in core-line XPS BEs are related to the interactions between an atom of interest and its nearest immediate neighbours, an effect known as the primary substituent shift [1]. Longer-range interactions with more distant atoms in secondary coordination shells may also exert an influence on these BEs, an effect known as the secondary substituent shift (also called β-shift or next-nearest neighbour shift) [1].

X-ray absorption spectroscopy (XAS) also provides information about the electronic structure of materials. This technique can be subdivided into X-ray absorption near-edge spectroscopy (XANES), which examines variations in energy and lineshape of the absorption edge, and extended X-ray absorption fine structure (EXAFS), which probes the local atomic structure [2,3]. Similar to XPS, the XANES absorption energy shifts as the local chemical environment is altered [2,3]. The lineshape reveals valuable information about the composition of the valence and conduction states [3]. Next-nearest neighbour effects have also been implicated in XANES spectra [4].

This next-nearest neighbour effect, examined by XPS, has been identified in a few specific cases. The clearest examples occur in halogenated hydrocarbons [1,5–7]. In fluorinated aromatic hydrocarbons, the substitution of H by F induces a positive shift in the C $1s$ XPS spectrum by as much as 3 eV for the α-C atoms (bound directly to F) and

*Corresponding author. Fax: +1 780 492 8231.
 E-mail address: andrew.grosvenor@ualberta.ca (A.P. Grosvenor).

by ~1 eV for the β-C atoms (those bound to the α-C). Molecular orbital calculations revealed that the BEs of the β-C atoms shift not only because of the change in electronegativity of the substituent F vs. H, but also because of the change in the charge developed on the α-C atoms [5]. The magnitude of this shift is thus expected to be less pronounced as the electronegativity of the substituent decreases, as has been observed in Cl-, Br-, O-, and N-containing polymers [8–11]. The source of the shifts can be identified using a simple model that describes the BE shifts arising from ground state effects. This model, called the charge potential model, is defined by the equation:

$$\Delta E_i = E_i - E_i^{\rm o} = k\Delta q_i + \Delta \sum_{j \neq i} q_j/r_{ij}. \qquad (1)$$

The total BE shift, ΔE_i, which is the difference between the measured BE of the atom of interest, E_i, and a reference BE, $E_i^{\rm o}$, consists of two contributions. The $k\Delta q_i$ term describes intraatomic effects involving the change in charge Δq_i on atom i multiplied by a constant k, which is related to the interaction between valence and core electrons [12,13]. The $\Delta\sum_{j \neq i}(q_j/r_{ij})$ term describes interatomic effects involving changes in the local chemical environment and, because of its similarity to the Madelung potential, is often referred to as such [12,13]. The charge potential model explains the BE shifts in the example above. When H is substituted by the more electronegative F atom, the α-C atom has a higher BE because its apparent positive charge q_i is increased. In turn, the increase in the apparent charge on the α-C atom induces a more positive Madelung potential felt by the β-C atom, whose BE also becomes higher [5]. This analysis indicates that intraatomic effects (i.e., change in charge) have a greater influence on the magnitude of the BE shift than do interatomic effects (i.e., change in Madelung potential).

Next-nearest neighbour effects have been observed in the XPS spectra for a few inorganic substances. In nitrided silicon dioxide and silicon oxynitride thin films, the N 1s BEs shift by ~0.1 eV upon substitution of the next-nearest neighbours (O for Si) [14,15]. The P 2p BEs of transition-metal substituted phosphate (P_2O_5) glasses decrease when the next-nearest neighbour is replaced by a metal (i.e., P–O–P to P–O–M) [16,17]. The magnitude of the shift (1–2 eV) diminishes as the electronegativity of the metal increases [16–19]. According to the charge potential model, when P is substituted by the more electropositive M atom, the apparent negative charge on the O atom increases not only because of a change in its formal charge but also in the degree of ionic bonding. This induces a more negative Madelung potential felt by the (unsubstituted) P atom, whose 2p BE becomes lower. Quantum chemical calculations for several sulphide minerals showed that the S 2p BEs depend on interactions with next-nearest neighbours when they are sufficiently close to the S atom [20]. For example, in MoS_2 (molybdenite), the calculated S 2p BE is 161.7 eV when only nearest neighbours are considered, but

is 162.5 eV when next-nearest neighbours are included, in excellent agreement with the range of experimentally reported values (162.0–162.8 eV) [20]. These observed differences in BE can be related to the expected change in the magnitude of the Madelung potential when both nearest and next-nearest neighbours are included in the calculation in contrast to the underestimate when only nearest neighbours are considered.

Recently, we have examined the XPS spectra of binary transition-metal phosphides MP (M = Cr, Mn, Fe, Co) with the MnP-type structure [21]. The metal atoms are coordinated to P atoms in a distorted octahedral geometry and establish metal–metal bonding (<3 Å) through zigzag chains along the a and b directions (Fig. 1) [22]. Mixed transition-metal phosphides $M_{1-x}M'_xP$ with the same structure type can also be prepared in which M and M' are randomly distributed in the metal sublattice, as indicated by the presence of sharp reflections and the absence of superstructure reflections in the X-ray and neutron diffraction patterns [23,24]. Both the binary and pseudobinary phosphides are metallic and display interesting magnetic properties [23–29]. They have also been examined as possible hydrodesulphurization and hydrodenitrogenation catalysts [30,31].

We report here the XPS spectra of several series of mixed phosphides ($Co_{1-x}Mn_xP$, $Mn_{1-x}V_xP$, and $Co_{1-x}V_xP$) and demonstrate how next-nearest neighbour contributions influence the P 2p BEs. The observed shifts in energies are described in terms of the charge potential model and electronegativity of the metals. An empirical model that combines both nearest and next-nearest neighbour contributions derived from electronegativity differences allows estimation of the magnitude of the shifts. Metal XPS and XANES spectra were also analysed as well as the P K-edge XANES spectra.
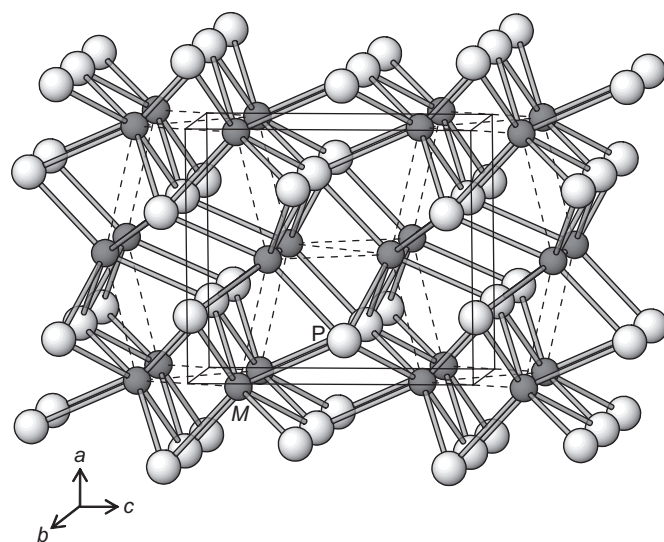

Fig. 1. MnP-type crystal structure viewed down the *b*-axis. The small solid spheres are M atoms and the large lightly shaded spheres are P atoms. The dashed lines indicate the metal–metal bonding network.

2. Experimental

2.1. Synthesis

Starting materials were powders of the metals (Ti, 99.98%, Cerac; V, 99.5%, Alfa-Aesar; Mn, 99.95%, Cerac; Co, 99.999%, Spex) and red P (99%, Alfa-Aesar). Products were identified by their powder X-ray diffraction patterns obtained on an Inel powder diffractometer equipped with a CPS 120 detector. All samples were manipulated and stored in a glove box under Ar to limit exposure to air.

The parent binary monophosphides (CoP, MnP, and VP) were prepared through stoichiometric reaction of metal powders with red P confined in evacuated fused-silica tubes. The tubes were heated up to 1323 K over 48 h and held at this temperature for 1 week before being cooled slowly over 24 h to room temperature. The end member, TiP, was similarly prepared through reaction of Ti powder and red P in an evacuated fused-silica tube heated to 1173 K over 36 h and held at this temperature for 1 week before being quenched in water.

The mixed metal phosphides ($Co_{1-x}Mn_xP$, $Mn_{1-x}V_xP$, and $Co_{1-x}V_xP$) were prepared from stoichiometric reaction of the binary phosphides. The mixed materials were ground together in a glove box under dry Ar and sealed in evacuated fused-silica tubes. The tubes were heated up to 1273 K over 20 h, held at this temperature for ~5 d, and then quenched in water. This heating and grinding process was repeated for a total of three 5-d heat treatments at 1273 K to improve the homogeneity of each sample. The following samples were examined by XPS and XANES analyses: $Co_{0.10}Mn_{0.90}P$, $Co_{0.30}Mn_{0.70}P$, $Co_{0.40}Mn_{0.60}P$, $Mn_{0.95}V_{0.05}P$, $Mn_{0.85}V_{0.15}P$, $Mn_{0.75}V_{0.25}P$, $Mn_{0.60}V_{0.40}P$, $Co_{0.90}V_{0.10}P$, and $Co_{0.80}V_{0.20}P$. Powder X-ray diffraction confirmed that these samples were single-phase and that all adopt the MnP-type structure. The $Co_{1-x}Mn_xP$ and $Mn_{1-x}V_xP$ series have been reported previously [23,24]. The $Co_{1-x}V_xP$ series is new (although the corresponding arsenide series, $Co_{1-x}V_xAs$, is known [32]), and the two members prepared have cell parameters ($a = 5.095(3)$ Å, $b = 3.268(3)$ Å, $c = 5.629(4)$ Å for $Co_{0.90}V_{0.10}P$ and $a = 5.106(3)$ Å, $b = 3.262(3)$ Å, $c = 5.658(4)$ Å for $Co_{0.80}V_{0.20}P$) that extrapolate smoothly from those of CoP ($a = 5.077$ Å, $b = 3.281$ Å, $c = 5.587$ Å) in accordance with Vegard's law [33]. The smooth variation in cell parameters vs. x (Fig. S1 in Supplementary Data) and the lack of peak broadening in the powder diffraction patterns (Table S1 in Supplementary Data) for the mixed-metal phosphides strongly support the presence of single-phase samples.

2.2. XPS analysis

Measurements were performed on a Kratos AXIS 165 spectrometer using either Mg K or Al K X-rays. The resolution function for this instrument has been determined to be 0.4 eV when monochromatic Al $K\alpha$ X-rays are used

based on analysis of the Co Fermi edge. Analysis of multiple Cu $2p_{3/2}$ spectra yielded a BE of 932.59 ± 0.03 eV indicating that the second decimal place is significant. This value agrees with those previously reported [34].

After the samples were finely ground in a glove box under Ar, they were pressed onto In foil (Alfa-Aesar) or C tape, and placed on a Cu sample holder. The samples were then transported to the XPS instrument under Ar to reduce the possibility of surface oxidation. After being loaded into the spectrometer, samples were sputter-cleaned for 30–60 min by means of Ar^+ ion sputtering (4 kV, 10 mA) to remove any surface oxide or phosphate formed. Analysis of the survey spectra collected indicated that only a small amount of phosphate remained after this procedure. Preferential sputtering of the light elements was not observed. High-resolution spectra of the P 2p, metal 2p, and C 1s core lines were collected with a pass energy of 20–40 eV, a step size of 0.05 eV, a sweep time of 180 s, and an energy envelope of 20–40 eV. Spectra were analysed with the aid of the CasaXPS software program [35]. During data analysis, the samples were calibrated using the C 1s line arising from adventitious C with a fixed value of 284.80 eV, although this was rarely required because the samples studied are metallic. To remove the background arising from energy loss, a Shirley-type function was applied.

2.3. P K-edge XANES analysis

XANES spectra of the P K-edge were collected at the Canadian Light Source (CLS), Saskatoon, Saskatchewan, using the spherical grating monochromator (SGM) undulator beamline, 11-ID.1. Although the P K edge is outside the design range of the beamline, good quality spectra were still obtained. At this energy, the monochromatized photon flux is ~10^9 photons/s, with an estimated resolution of ~1 eV and a beam size of approximately 50×100 μm. Powdered samples were mounted on carbon tape and inserted in the vacuum chamber via a load lock. Total electron yield and total X-ray fluorescence yield spectra were measured from 10 eV below the edge to ~35 eV above the edge at 0.1 eV per step. The spectra were calibrated against a sample of $Na_4P_2O_7$, with the peak maximum of the P K-edge set to 2152.4 eV [36]. The P edge values reported herein represent the maximum of the first-derivative peak of each spectrum which removes the influence of higher energy surface phosphates. A precision of ± 0.1 eV was estimated through comparison of multiple analyses of the compounds studied.

2.4. Mn K-edge XANES analysis

XANES spectra of the Mn K-edge were collected at Pacific Northwest Consortium/X-ray Operations and Research Collaborative Access Team (PNC/XOR-CAT), Sector 20 at the Advanced Photon Source (APS), Argonne National Laboratory with the bending magnet (20BM)

beamline. A silicon (111) double crystal monochromator was used to provide a monochromatic photon flux of $\sim 10^{11}$ photons/s, with a resolution of 1.4 eV at 10 keV and a beam size of approximately 1×5.5 mm. Powdered samples were ground, sandwiched between Kapton tape, and positioned 45° to the X-ray beam. The fluorescence spectrum was measured with a Lytle-type fluorescence ionization chamber detector positioned at 90° relative to the X-ray beam [37]. Through the absorption edge, the X-ray energy was increased by 0.25 eV per step. A Mn metal standard was positioned behind the sample and analysed concurrently in transmission mode using N_2-filled ionization chambers. The resulting K-edge was calibrated to the accepted value of 6539 eV. All XANES spectra were analysed using the Athena software program [38].

3. Results and discussion

3.1. P 2p XPS spectra

P 2p spectra were collected for several binary (MnP, CoP) and pseudobinary mixed ($Co_{1-x}Mn_xP$, $Mn_{1-x}V_xP$, and $Co_{1-x}V_xP$) phosphides with the MnP-type structure, as well as for TiP (TiAs-type) and VP (NiAs-type). These structure types are closely related and differ only in the extent of small structural distortions [39]. Because the P 2p spectra for all samples are similar, it suffices to show representative examples, such as MnP and $Mn_{0.85}V_{0.15}P$, as presented in Fig. 2. In general, the separation between the $2p_{3/2}$ and $2p_{1/2}$ peaks for the parent binary phosphide (MnP) is clear (Fig. 2a), but it is less obvious for the mixed phosphide ($Mn_{0.85}V_{0.15}P$) (Fig. 2b). The FWHM of the component peaks required to fit the spectra increases from 0.7 eV for MnP to 0.9 eV for $Mn_{0.85}V_{0.15}P$. The line broadening in $Mn_{0.85}V_{0.15}P$ can be ascribed to the superposition of multiple signals arising from the presence of different local distributions of metal atoms around each P atom. Nevertheless, it is still a reasonable approximation to fit the spectra of the mixed phosphides with single $2p_{3/2}$ and $2p_{1/2}$ component peaks to determine average BEs.

Fig. 3a shows a plot of the P $2p_{3/2}$ BEs (also listed in Table 1) for various binary (MP) and mixed ($M_{1-x}M'_xP$) phosphides. The BEs are reported to two decimal places with a reliability of better than ± 0.10 eV based on multiple analyses of separately synthesized samples or the same sample examined at different times (Table S2 in Supplementary Data). The horizontal axis represents the difference in Allred-Rochow electronegativity between phosphorus and the metal ($\chi_P - \chi_M$) [40]. In the case of the mixed phosphides, χ_M is replaced by the weighted average electronegativity of the two metals, $(1-x)\chi_M + x\chi_{M'}$. This type of plot has been applied previously to examine trends in bonding character as the electronegativity difference between the metal and ligand is altered in a series of related compounds [21,41,42]. For the binary phosphides MP, the P $2p_{3/2}$ BEs decrease linearly on progressing from CoP to TiP. This trend is consistent with expectations: as M
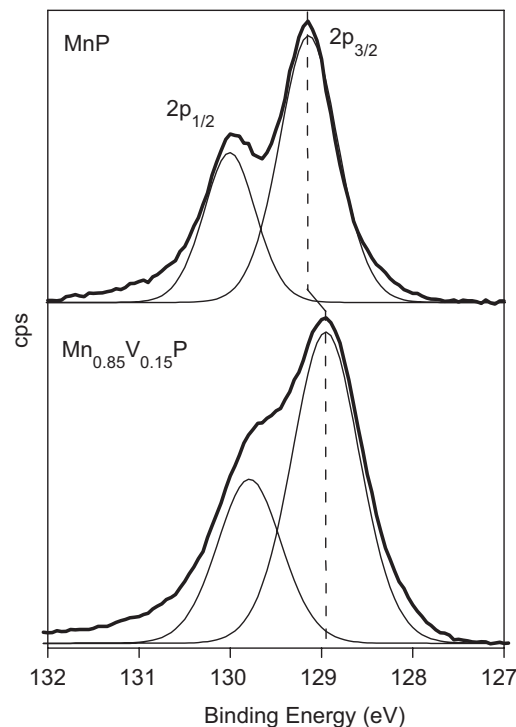

Fig. 2. High-resolution P 2p spectra for (a) MnP and (b) $Mn_{0.85}V_{0.15}P$. The MnP spectrum was given in Ref. [21]. Each spectrum has been fitted with two peaks representing the $2p_{3/2}$ and $2p_{1/2}$ spin-orbit final states in a 2:1 intensity ratio and the background has been subtracted using a Shirley-type function. The $2p_{3/2}$ binding energies are indicated by vertical dashed lines and are also provided in Table 1.

becomes more electropositive, the greater ionic character of the M–P bonds induces a more pronounced electron transfer to P, which gains more electron density. If Eq. (1) is applied to the binary phosphides MP, the charge potential model predicts that the phosphorus BE will be lowered by the enhanced negative charge q_i on P, but raised by the more positive Madelung potential arising from the enhanced positive charge on the surrounding metal atoms. The observed trend of an overall linear decrease in BE from CoP to TiP confirms that intraatomic effects tend to dominate over interatomic effects, as asserted earlier. In contrast, however, the BEs for the mixed phosphides $M_{1-x}M'_xP$ do not follow this linear trend, and instead are lower than expected relative to those of the binary phosphides MP.

To understand why the mixed phosphides $M_{1-x}M'_xP$ behave differently, we must consider the complete crystal structure. In the MnP-type structure, adopted by the compounds studied here, each metal atom is surrounded by six nearest-neighbour P atoms at distances of 2.2–2.4 Å which define the immediate first coordination shell [22]. There are, however, four other metal atoms in the coordination environment, at slightly longer distances of 2.6–2.8 Å [22]. These form part of a metal–metal bonding network which must also be considered. In the binary phosphides MP, all the metal atoms are the same, but in the mixed phosphides $M_{1-x}M'_xP$, it is possible for an M
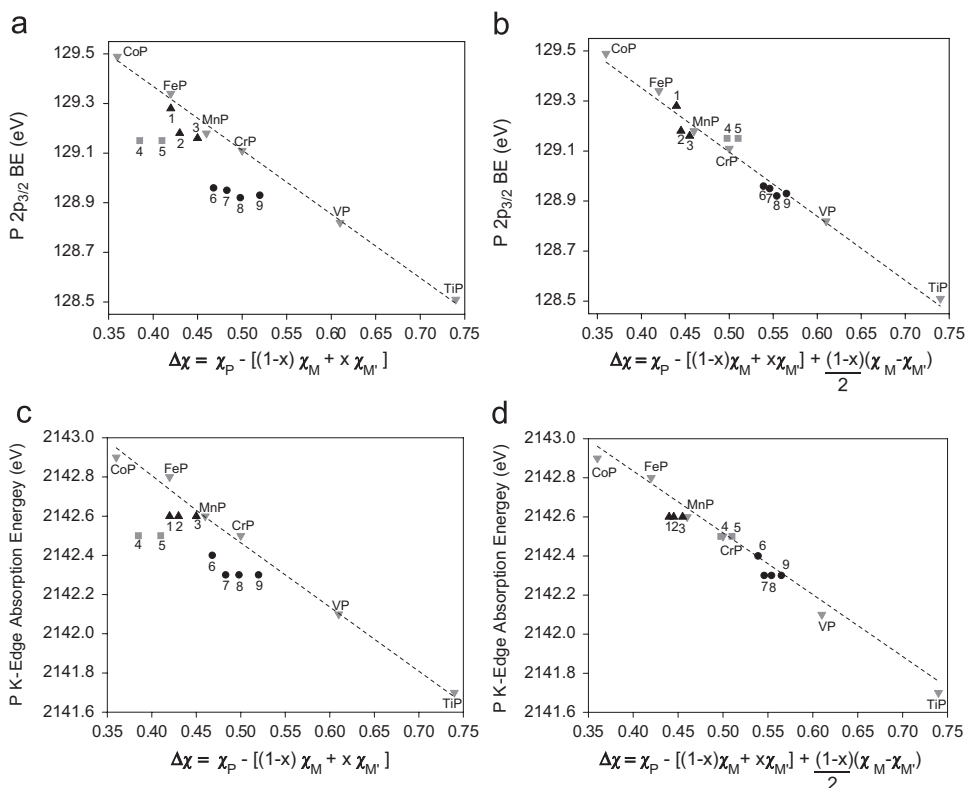
Fig. 3. Dependence of (a–b) P $2p_{3/2}$ binding energy and (c–d) P K-edge absorption energy on electronegativity difference $\Delta\chi$ for binary phosphides MP ($\blacktriangledown$) and ternary phosphides $Co_{1-x}Mn_xP$ ($\blacktriangle$) ($1 = Co_{0.40}Mn_{0.60}P$, $2 = Co_{0.30}Mn_{0.70}P$, $3 = Co_{0.10}Mn_{0.90}P$), $Co_{1-x}V_xP$ ($\blacksquare$) ($4 = Co_{0.90}V_{0.10}P$, $5 = Co_{0.80}V_{0.20}P$), and $Mn_{1-x}V_xP$ ($\bullet$) ($6 = Mn_{0.95}V_{0.05}P$, $7 = Mn_{0.85}V_{0.15}P$, $8 = Mn_{0.75}V_{0.25}P$, $9 = Mn_{0.60}V_{0.40}P$). Binding energies for CoP, FeP, MnP, and CrP are from Ref. [21]. The expression for $\Delta\chi$ incorporates only nearest neighbour contributions (Eq. (2)) in (a) and (c), but also includes next-nearest neighbour contributions (Eq. (3)) in (b) and (d), leading to improved correlations as seen by the linear fits to the data (dashed lines) with $R^2 = 0.971$ and 0.982, respectively.

Table 1
Phosphorus $2p_{3/2}$ binding energies, P K-edge absorption energies, and metal $2p_{3/2}$ binding energies for metals, binary phosphides MP, and mixed phosphides $M_{1-x}M'_xP$

Compound	P $2p_{3/2}$ BE (eV)	P K-edge absorption energy (eV)	Co $2p_{3/2}$ BE (eV)	Mn $2p_{3/2}$ BE (eV)	V $2p_{3/2}$ BE (eV)
Co			778.10		
Mn				638.66	
V					512.3 ± 0.1
CoP	129.49	2142.9	778.33		
FeP	129.34	2142.8			
MnP	129.18	2142.6		638.73	
CrP	129.11	2142.5			
VP	128.82	2142.1			512.50
TiP	128.51	2141.7			
$Co_{0.10}Mn_{0.90}P$	129.16	2142.6	778.49	638.78	
$Co_{0.30}Mn_{0.70}P$	129.18	2142.6	778.41	638.78	
$Co_{0.40}Mn_{0.60}P$	129.28	2142.6	778.35	638.78	
$Co_{0.90}V_{0.10}P$	129.15	2142.5	778.10		512.48
$Co_{0.80}V_{0.20}P$	129.15	2142.5	778.15		512.54
$Mn_{0.95}V_{0.05}P$	128.96	2142.4		638.72	512.55
$Mn_{0.85}V_{0.15}P$	128.95	2142.3		638.63	512.49
$Mn_{0.75}V_{0.25}P$	128.92	2142.3		638.65	512.47
$Mn_{0.60}V_{0.40}P$	128.93	2142.3		638.70	512.50

Values for Co, Mn, CoP, FeP, MnP, and CrP were taken from Ref. [21]. The V metal $2p_{3/2}$ binding energy was taken from Ref. [34]. The P K-edge absorption energies were determined from the fluorescence spectra collected at the CLS and calibrated against a $Na_4P_2O_7$ standard.

atom to be surrounded locally not only by other M atoms but also by M' atoms, particularly when x is large. As a result, a polarization develops between the two different metals. If M is designated as the more electronegative metal and M' as the more electropositive metal in the formula $M_{1-x}M'_xP$, then M' will donate electron density not only to the P atoms but also to the M atoms. The M atoms in $M_{1-x}M'_xP$ then acquire more electron density than they possess in the parent binary compound MP. The apparent charge of the M atoms decreases as a result of this charge transfer. Within the charge potential model, this will affect the P $2p$ BEs by altering the Madelung potential term $(\Delta\sum_{j\neq i}(q_j/r_{ij}))$. If the P $2p_{3/2}$ BEs of the mixed metal phosphides are compared to the line of best fit presented in Fig. 3a for the binary phosphides, it can be seen that the deviation in BE tends to become more negative with increasing concentration of M atoms. This can be ascribed to an overall decrease in Madelung potential owing to the $M'\rightarrow M$ charge transfer (i.e. q_M decreases which lowers $\Delta\sum_{j\neq i}(q_j/r_{ij})$ at high concentrations of M). In this series, there is also a change in the average M–P bond lengths, ranging from 2.304 Å in CoP to 2.358 Å in MnP [22]. As a result of the $1/r_{ij}$ dependence, the charge on the smaller, more electronegative M atoms has a greater influence than the larger, more electropositive atoms M' in the Madelung potential term.

The next-nearest neighbour effect described here can be compared with those described in the introduction. It is similar to the case of phosphate glasses in which substitution of P with a metal (with O located between the P atom under examination and the substituted atom; i.e., P–O–M) causes a decrease in the P $2p$ BE [16–19]. In these phosphate glasses, the substitution of P with M alters the Madelung potential component of the P $2p$ BE causing it to be lower than it is in the unsubstituted case. In this example and those presented in the introduction, the *identity* of the nearest neighbour is important in describing the shift in BE (in terms of both magnitude and direction) experienced because of next-nearest neighbour effects.

To improve the correlation of the P $2p$ BE shift trends with atomic properties for the $M_{1-x}M'_xP$ system, we have extended the model to include next-nearest neighbour contributions employing a simple electronegativity analysis. To derive Fig. 3a we had assumed that, as in the binary phosphides MP, the magnitude of the ground state transfer of electron density from the metal to the P atoms in the first coordination shell was related to the difference in electronegativity of P and of the weighted average of the metals:

$$\Delta\chi = \chi_P - [(1-x)\chi_M + x\chi_{M'}]. \qquad (2)$$

In the context of the charge potential model, Eq. (2) incorporates the change in the apparent charge on the P atoms (Δq_i) because of the substitution of one metal for another. Much of the change can be related to the variation in degree of ionic bonding present as a metal of different electronegativity is substituted for the original. The lower than expected P $2p_{3/2}$ BE values for $M_{1-x}M'_xP$ relative to

those for MP (Fig. 3a) and the fact that these shifts do not fall on the line connecting the simple binaries suggest that $\Delta\chi$ should be increased to achieve a linear correlation. Increasing $\Delta\chi$ results naturally when a term to represent the charge transfer occurring between M and M', i.e. $\chi_M-\chi_{M'}$, is added to Eq. (2). Introducing this next level of charge readjustment alters the Madelung potential term, which is $\Delta\sum_{j\neq i}(q_j/r_{ij})$ in the charge potential model. Because the level of substitution, x, varies through a given $M_{1-x}M'_xP$ series, $\chi_M-\chi_{M'}$ must be multiplied by a scaling factor that reflects the proportionate degree of this additional charge transfer. It is the concentration of the more electronegative metal M that is most important because M receives electron density from M', reducing the charge (q_j) on M, which results in an overall decrease in the Madelung potential and thus a lowering of the P $2p$ BE. As was indicated above, the magnitude of this shift increases with increasing concentration of M. The fractional concentration of M atoms is $(1-x)$ relative to all metal atoms, but because only one out of every two atoms in the formula $M_{1-x}M'_xP$ is a metal, this must be divided by two to give the concentration of M relative to all atoms. Thus, the final expression for the difference in electronegativity is

$$\Delta\chi = \chi_P - [(1-x)\chi_M + x\chi_{M'}] + \frac{(1-x)}{2}(\chi_M - \chi_{M'}). \qquad (3)$$

For the parent binary phosphides MP for which $x = 0$ and $M = M'$, the expression reduces to the simple difference in electronegativity between M and P. In those cases, the change in q_i (the charge on P) correlates directly with the magnitude of the P $2p$ BE shift.

Fig. 3b shows a plot of the P $2p_{3/2}$ BEs vs. the extended expression for the electronegativity difference for the MP and $M_{1-x}M'_xP$ phosphides which takes next-nearest neighbour effects into consideration. The linear correlation ($R^2 = 0.971$) lends strong support to this model in which both nearest and next-nearest neighbour effects are included. Additional compelling evidence is provided by comparing the plots of the P K-edge absorption energies (Table 1) vs. the electronegativity difference calculated using either Eq. (2) (Fig. 3c) or Eq. (3) (Fig. 3d). Representative P K-edge XANES spectra from CoP and $Co_{0.80}V_{0.20}P$ are presented in Fig. 4. Because XANES is a bulk-sensitive technique, the agreement between the XANES and XPS results indicates that the variations in P $2p$ BE observed between the binary and mixed-metal phosphides derive from a bulk rather than a surface electronic effect. The excellent correlation obtained when Eq. (3) is applied to the P K-edge absorption energies reinforces the importance of next-nearest neighbour contributions when the second coordination shell has been modified by substitution.

Although the charge potential model describes the variations in P BE and absorption energy well in this system, it should be emphasized that this model is based only on changes in ground state energies. In reality, the BE of the X-ray excited photoelectron represents the difference
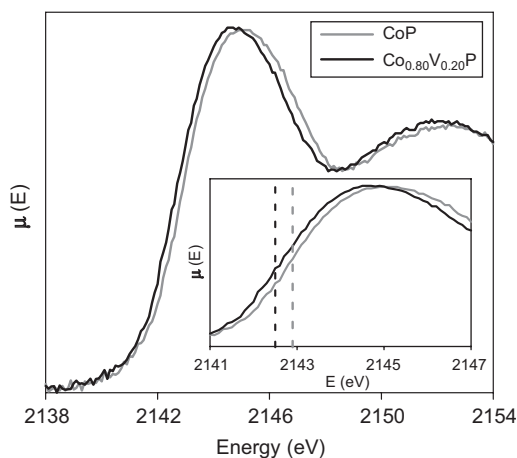
Fig. 4. P K-edge XANES spectra for CoP and $Co_{0.80}V_{0.20}P$ representing P $1s \rightarrow np$ transitions. Inset: Absorption edges with the inflection points (Table 1) marked by vertical dashed lines.

in energy between the ground state of the atom having n electrons and the final state of the atom containing $n-1$ electrons [20]. As such, various processes can affect the final state energy and therefore alter the BE of the atom under study. The presence of a hole in the core electron states produced by the removal of a photoelectron can be thought to act like a positive charge. One of the effects of this added unit of positive charge is adiabatic relaxation of the electrons towards the nucleus which can be separated into inter- and intra-atomic contributions [1]. An increase of electron density flowing toward the atom due to the production of the core-hole acts to decrease the final state energy by increasing the screening of the nuclear charge; this results in a lowering of the BE of the atom under study [1]. The resulting reorganization of the distribution of electron density on the surrounding atoms will also alter the Madelung potential component of the final state [20]. Analysis of the relaxation energy of gas-phase P and S compounds suggests that when the coordination environment around a given atomic centre is fixed (as is the case in the metal phosphides discussed here), greater relaxation occurs as the electronegativity of the ligand decreases [43,44]. By comparison to the P 2p BEs presented above, if relaxation was responsible for the shifts in energy observed in the $M_{1-x}M'_xP$ compounds, then the magnitude of the shift would be expected to increase with increasing concentration of M' (the more electropositive metal). However, the situation is reversed in that the magnitude of the shift decreases with increasing concentration of M'. This suggests then that variations in adiabatic relaxation are not responsible for the shifts found in these mixed metal compounds compared to the binary phosphides. Given this conclusion, it is reasonable to use the charge potential model to describe the observed variations in the P 2p BEs, particularly since it has been found that variations in the Madelung potential tend to have a larger influence on the BE than do changes in adiabatic relaxation [45,46].

3.2. Metal 2p XPS spectra

Fig. 5 shows a collection of metal $2p_{3/2}$ spectra for the parent binary phosphides MP and several representative members of the $M_{1-x}M'_xP$ series. All spectra exhibit an asymmetric lineshape, which is characteristic of an itinerant electronic structure as first described by Doniach and Šunjić [47]. This type of lineshape arises when valence electrons, interacting with the core hole (produced by photoionization), are excited and scattered from filled states below the Fermi edge to empty conduction states above. Since there is a continuum of states above the Fermi edge in metallic compounds such as those investigated here, an asymmetric tail comprising many closely spaced states is observed instead of a few distinct satellite peaks [48]. As previously observed in the parent binary compounds [21], the delocalized electronic structure of the metal atoms arises from the strong metal–metal bonds found in phosphides with the MnP-type structure. Table 1 lists the metal $2p_{3/2}$ BEs for the elemental metals, the binary phosphides MP, and the mixed phosphides $M_{1-x}M'_xP$. In contrast to the P spectra, the metal $2p_{3/2}$ BEs generally do not shift appreciably in $M_{1-x}M'_xP$ relative to those in the parent binary phosphides. The electronic delocalization arising from metal-metal bonding in $M_{1-x}M'_xP$ leads to a well-screened final state (as is found in the parent compounds as well as in the elemental metals) that is produced after photoionization, so that little variation in the metal $2p_{3/2}$ BEs is observed. Unlike for the P 2p spectra, this is a situation where the charge potential model is unable to describe the BE shifts properly, because final state effects such as those described above are not incorporated into Eq. (1).

Unlike the other mixed phosphides, the $Co_{1-x}V_xP$ series appears to be anomalous in displaying perceptible differences in the Co $2p_{3/2}$ BEs relative to those in CoP (see Table 1 and Fig. 5). In $Co_{0.90}V_{0.10}P$ and $Co_{0.80}V_{0.20}P$, the Co $2p_{3/2}$ BE is ~0.2 eV lower than in CoP, whereas the V $2p_{3/2}$ BE is nearly identical to that in VP. The appearance of a shift in the case of the Co 2p BEs of $Co_{1-x}V_xP$ compared to CoP, in contrast to the constancy of metal 2p BEs throughout the parent and mixed metal phosphides, can be ascribed to the magnitude of the differences in metal electronegativities, $\chi_M - \chi_{M'}$. As indicated above, this quantity relates directly to the change in charge experienced by M. The electronegativity difference between Co and V is the largest ($\chi_{Co} - \chi_V = 0.25$); in the other cases, the differences are smaller ($\chi_{Mn} - \chi_V = 0.15$ and $\chi_{Co} - \chi_{Mn} = 0.10$ [40]). The downward shift in BE observed for the Co 2p spectrum of $Co_{1-x}V_xP$ compared to CoP confirms the charge transfer model above. This result shows how substitution of Co (M) for V (M') can cause a decrease in the Madelung potential term of the local environment around the P atoms through a reduction of the charge on the M atoms.

The satellite peak observed in the Co $2p_{3/2}$ spectra at an energy slightly higher than the main core-line (Fig. 5c) also

provides support for the proposed charge transfer that occurs from $M' \rightarrow M$ in the mixed metal phosphides as a result of the metal–metal bonding framework. In a
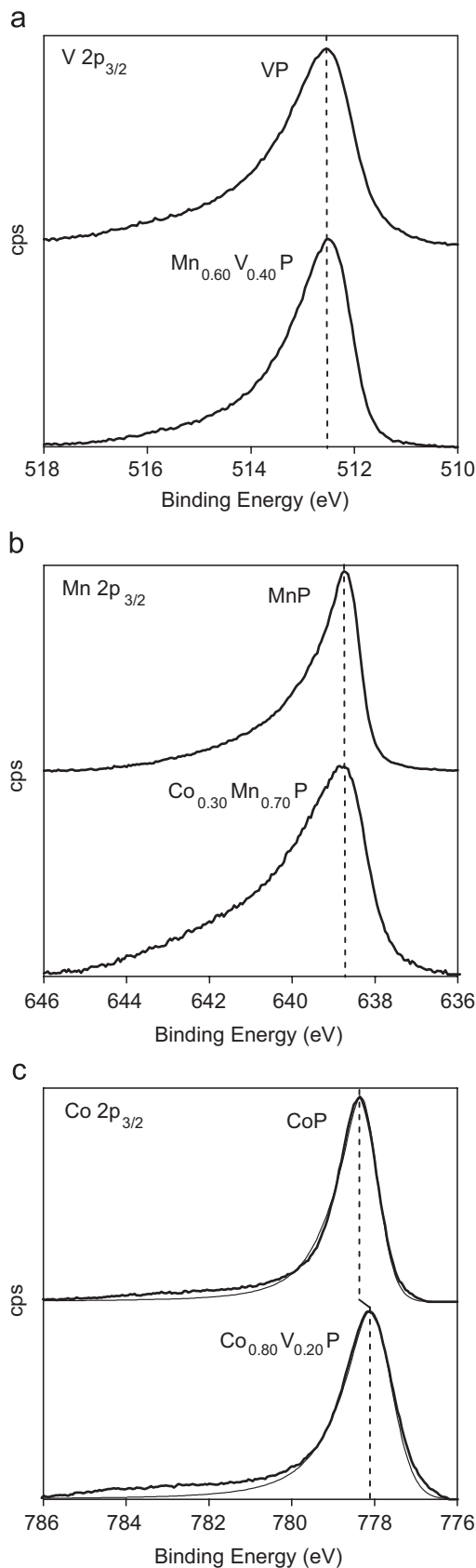
previous report, we have attributed this satellite peak to plasmon loss [21]. Plasmon loss can be described as the loss of kinetic energy of the photoelectron (increase in BE) arising from an oscillation of bound valence electrons [49]. This assignment has been corroborated by identifying the occurrence of the same phenomenon in most of the first-row transition metals (Sc–Ni) [50–54]. Note that no such plasmon loss peak is observed in the Mn or V $2p_{3/2}$ spectra, likely because it is overlapped by the significantly more intense core-line. The amplitude of the plasmon loss peak observed in the Co $2p_{3/2}$ spectra has been shown to vary greatly with only a slight change in the occupancy of the Co valence states [21,55]. Analysis of the 1s XPS peak of the series Sc–Co using a Cu $K\alpha$ X-ray source also revealed that the plasmon loss peak intensifies with greater number of spin-unpaired electrons, and that the energy separation between the plasmon loss peak and the core-line increases with greater concentration of $3d$ valence electrons [54]. The intensity of the plasmon loss peak is more sensitive than the energy of the plasmon loss peak or the $2p_{3/2}$ core-line BE to changes in the occupancy of the valence states. For example, the plasmon peak is considerably more intense but is only 0.3 eV higher in energy in the Co $2p_{3/2}$ spectrum for Co metal vs. that in CoP [21], and the Co $2p_{3/2}$ BE differs by only 0.2 eV on progressing from Co to CoP (see Table 1 and Ref. [21]) owing to electronic delocalization.

In comparison to CoP and $Co_{1-x}Mn_xP$, the satellite peak for $Co_{1-x}V_xP$ is significantly more intense. To quantify this observation, Fig. 6 shows a plot of the normalized intensity of the plasmon loss peak ($I_{plasmon}/I_{core-line}$) vs. the difference in electronegativity between the metals ($\chi_M - \chi_{M'}$). For reference, the normalized intensity of the plasmon loss peak for Co metal is shown as a dashed line. As the electronegativity difference increases, the plasmon loss peak intensifies. The plot reveals that Co atoms in $Co_{1-x}V_xP$ contain significantly more electron density in their valence states than is the case for CoP. An increase in occupation of the Co valence states is also observed within the $Co_{1-x}Mn_xP$ series. These results further support the argument that as Co is substituted for a more electropositive metal, its charge decreases, thereby reducing the Madelung potential term operating on the P $2p$ BE which is lowered compared to the binary phosphides. The intensity of the plasmon loss peak can also be related to the deviation of the P $2p_{3/2}$ (Fig. 3a) or P K-edge absorption energies (Fig. 3c) for $Co_{1-x}V_xP$ and $Co_{1-x}Mn_xP$. The more intense plasmon loss peak in $Co_{1-x}V_xP$ suggests a greater occupancy of Co valence states and lower Co charge than in $Co_{1-x}Mn_xP$. This is consistent with the more pronounced negative deviations

Fig. 5. Representative metal $2p_{3/2}$ spectra for $Mn_{1-x}V_xP$, $Co_{1-x}Mn_xP$, $Co_{1-x}V_xP$, and the parent binary phosphides. The spectra for CoP and MnP are from Ref. [21]. An asymmetric peak (thin solid line) has been used to fit the Co $2p_{3/2}$ spectra of CoP and $Co_{0.8}V_{0.2}P$, revealing the superimposed high binding energy satellite peak. The $2p_{3/2}$ binding energies, which are listed in Table 1, are marked by vertical dashed lines.
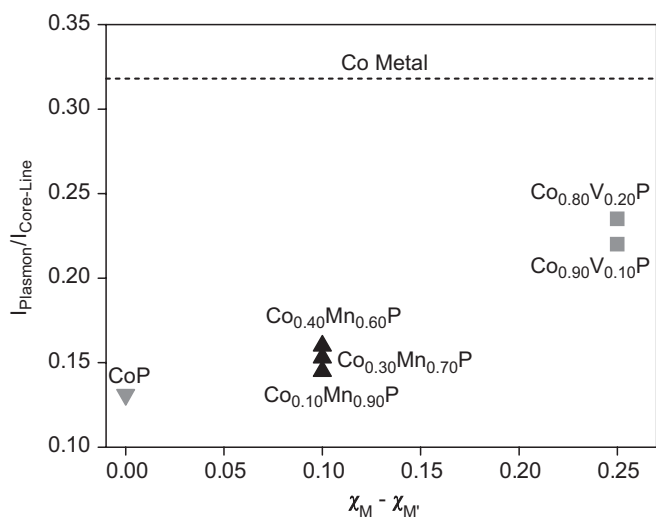
Fig. 6. Plot showing the variation in the normalized plasmon intensity vs. the difference in electronegativity between the two dissimilar metals ($\chi_M - \chi_{M'}$) in the Co 2p spectrum of CoP, $Co_{1-x}Mn_xP$, and $Co_{1-x}V_xP$. The value for Co metal is represented as a dashed line. The CoP and Co metal values are from Ref. [55].

of the P $2p_{3/2}$ and P K-edge absorption energies in $Co_{1-x}V_xP$ than in $Co_{1-x}Mn_xP$, as a result of the lowered Madelung potential in the case of the former.

3.3. Mn K-edge XANES

Because the Mn 2p XPS spectrum does not contain an observable plasmon loss peak, other methods must be used to interrogate the change in occupation of the Mn valence states in the $Mn_{1-x}V_xP$ and $Co_{1-x}Mn_xP$ series compared to MnP. The Mn K-edge XANES spectrum of MnP has been shown previously to contain a pre-edge peak arising from the excitation of 1s electrons into 3d states [56]. Among other factors, the intensity of this peak decreases with increasing occupancy of the metal 3d valence states [57]. Although the pre-edge peak is primarily assigned to a $1s \rightarrow 3d$ transition, the distorted octahedral coordination of the metal atoms in the MnP-type structure introduces some participation of 4p orbitals in the metal-phosphorus bonding [58] adding a small dipolar component ($1s \rightarrow 4p$) to this peak. As such, only compounds that are very similar to the parent binary can be compared, because any significant change in the P–M–P bond angles will alter the contribution of 4p orbitals involved in bonding and hence the intensity of the pre-edge peak. Moreover, quadrupolar $1s \rightarrow 3d$ transitions are already considerably weaker than dipolar ($1s \rightarrow 4p$) transitions [59]. For this reason, only the least substituted members where the structures are minimally perturbed ($Mn_{0.95}V_{0.05}P$ and $Co_{0.10}Mn_{0.90}P$) were examined, and their Mn K-edge XANES spectra are shown normalized in comparison to MnP in Fig. 7.

In $Mn_{0.95}V_{0.05}P$, the pre-edge peak (labelled A) is slightly less intense than in MnP (Fig. 7a). This indicates an

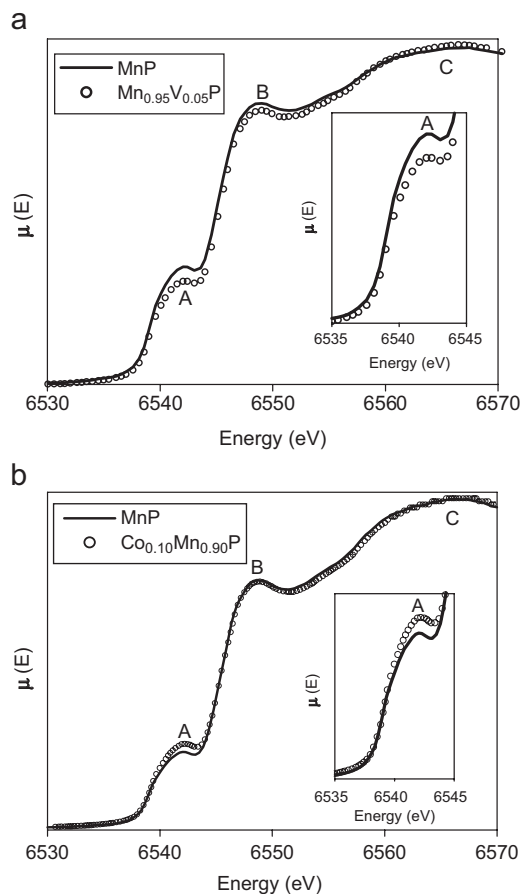Fig. 7. Mn K-edge XANES spectra of (a) $Mn_{0.95}V_{0.05}P$ and (b) $Co_{0.10}Mn_{0.90}P$. Included for comparison, the spectrum of MnP matches that reported previously [56]. Peak **A** represents the pre-edge peak originating from $1s \rightarrow 3d$ and $1s \rightarrow 4p$ transitions, peak **B** represents the excitation of Mn 1s electrons into P 3p antibonding states, and peak **C** represents the Mn $1s \rightarrow 4p$ transition [56]. The insets highlight details near peak **A**. The linewidths of the spectra are all broader than the standard deviation of the measurement.

increased occupancy of the Mn valence states in $Mn_{0.95}V_{0.05}P$ relative to MnP, providing further evidence for the occurrence of a secondary charge transfer from V to the more electronegative Mn atoms. In $Co_{0.10}Mn_{0.90}P$, the roles of the metal atoms are reversed relative to $Mn_{0.95}V_{0.05}P$, and charge transfer from the more electropositive Mn atoms to Co is now operative. The Mn K-edge spectra of $Co_{0.10}Mn_{0.90}P$ and MnP overlap well except for the region near the pre-edge peak (Fig. 7b). The slightly more intense pre-edge peak in $Co_{0.10}Mn_{0.90}P$ indicates decreased electron density of the Mn valence states compared to MnP. This observation agrees with the earlier conclusion that the Co valence states experience a slight increase in electron density, which manifests itself as an enhancement of the Co 2p plasmon loss peak in the $Co_{1-x}Mn_xP$ series (Fig. 6). That is, the charge transfer from Mn to Co is confirmed. This result is also consistent with the improved fitting of the P energies when Eq. (3) is used instead of Eq. (2) for the electronegativity expression, supporting the importance of next-nearest neighbour

contributions to alteration of the Madelung potential of the chemical environment surrounding the P atoms.

4. Conclusions

P $2p_{3/2}$ BEs and P K-edge absorption energies in mixed transition-metal phosphides $M_{1-x}M'_xP$ with the MnP-type structure are shifted down relative to those in the parent binary phosphides MP. These shifts arise from a next-nearest neighbour contribution which modifies the charge distribution. Charge transfer between the two dissimilar metals in $M_{1-x}M'_xP$ through a metal–metal bonding framework enables the more electronegative metal M atoms to acquire more electron density than is present in the parent binary compound MP. In terms of the charge potential model (Eq. (1)), this decreased positive charge on M acts to lower the Madelung potential of the environment around the P atoms, which is manifested by a lower P $2p_{3/2}$ BE and P K-edge absorption energy. The observed P shifts, which increase with increasing concentration of M, arises from both nearest and next-nearest neighbour interactions and can be modeled through an enhanced expression for the electronegativity difference (Eq. (3)) which necessarily must include the next-nearest neighbour contributions in differentially substituted systems. The modified electronegativity difference model correlates well with observed BEs.

Appendix A. Supplementary data

Supplementary data associated with this article can be found in the online version at doi:10.1016/j.jssc.2007.07.027.

References

[1] D. Briggs, Surface Analysis of Polymers by XPS and Static SIMS, Cambridge University Press, Cambridge, 2005.
[2] J.J. Rehr, R.C. Albers, Rev. Mod. Phys. 72 (2000) 622–654.
[3] J. Wong, F.W. Lytle, R.P. Messmer, D.H. Maylotte, Phys. Rev. B 30 (1984) 5596–5610.
[4] A. Mottana, A. Marcelli, G. Giuli, Z. Wu, F. Seifert, E. Paris, Phys. Chem. Miner. 23 (1996) 227–228.
[5] D.T. Clark, D. Kilcast, J. Chem. Soc. B: Phys. Org. Chem. (1971) 2243–2247.
[6] D.T. Clark, W.J. Feast, D. Kilcast, W.K.R. Musgrave, J. Polym. Sci.: Polym. Chem. Ed. 11 (1973) 389–411.
[7] R.J. Meier, Chem. Phys. Lett. 138 (1987) 471–475.
[8] A.P. Pijpers, W.A.B. Donners, J. Polym. Sci.: Polym. Chem. Ed. 23 (1985) 453–462.
[9] R.J. Meier, A.P. Pijpers, Theor. Chim. Acta 75 (1989) 261–270.
[10] D. Briggs, G. Beamson, Anal. Chem. 64 (1992) 1729–1736.
[11] D.T. Clark, H.R. Thomas, J. Polym. Sci.: Polym. Chem. Ed. 16 (1978) 791–820.
[12] P.A.W. van der Heide, Surf. Sci. 490 (2001) L619–L626.
[13] P.A.W. van der Heide, J. Electron Spectrosc. Relat. Phenom. 151 (2006) 79–91.
[14] J.R. Shallenberger, D.A. Cole, S.W. Novak, J. Vac. Sci. Technol. A 17 (1999) 1086–1090.
[15] D. Bouvet, P.A. Clivaz, M. Dutoit, C. Coluzza, J. Almeida, G. Margaritondo, F. Pio, J. Appl. Phys. 79 (1996) 7114–7122.
[16] M.A. Salim, G.D. Khattak, P.S. Fodor, L.E. Wenger, J. Non-Cryst. Solids 289 (2001) 185–195.
[17] B.V.R. Chowdari, K.L. Tan, W.T. Chia, R. Gopalakrishnan, J. Non-Cryst. Solids 119 (1990) 95–102.
[18] G.D. Khattak, M.A. Salim, L.E. Wenger, A.H. Gilani, J. Non-Cryst. Solids 262 (2000) 66–79.
[19] G.D. Khattak, M.A. Salim, A.S. Al-Harthi, D.J. Thompson, L.E. Wenger, J. Non-Cryst. Solids 212 (1997) 180–191.
[20] A.R. Gerson, T. Bredow, Surf. Interface Anal. 29 (2000) 145–150.
[21] A.P. Grosvenor, S.D. Wik, R.G. Cavell, A. Mar, Inorg. Chem. 44 (2005) 8988–8998.
[22] S. Rundqvist, P.C. Nawapong, Acta Chem. Scand. 19 (1965) 1006–1008.
[23] H. Fjellvåg, A. Kjekshus, Acta Chem. Scand. Ser. A 38 (1984) 563–573.
[24] H. Fjellvåg, A. Kjekshus, Acta Chem. Scand. Ser. A 38 (1984) 703–710.
[25] K. Selte, H. Fjellvåg, A. Kjekshus, Acta Chem. Scand. Ser. A 33 (1979) 391–395.
[26] H. Fjellvåg, A. Kjekshus, Acta Chem. Scand. Ser. A 38 (1984) 1–13.
[27] F. Hulliger, Struct. Bonding 4 (1968) 83–229.
[28] E.E. Huber Jr., D.H. Ridgley, Phys. Rev. [Sect.] A 135 (1964) 1033–1040.
[29] J. Okabayashi, K. Tanaka, M. Hashimoto, A. Fujimori, K. Ono, M. Okusawa, T. Komatsubara, Phys. Rev. B: Condens. Matter Mater. Phys. 69 (2004) 132411/1–132411/4.
[30] S.T. Oyama, J. Catal. 216 (2003) 343–352.
[31] X. Wang, P. Clark, S.T. Oyama, J. Catal. 208 (2002) 321–331.
[32] I.L. Andreassen, K. Selte, A. Kjekshus, Acta Chem Scand. Sect. A 31 (1977) 421–422.
[33] A.R. Denton, N.W. Ashcroft, Phys. Rev. A. 43 (1991) 3161–3164.
[34] C.D. Wagner, A.V. Naumkin, A. Kraut-Vass, J.W. Allison, C.J. Powell, J.R. Rumble Jr., NIST X-ray Photoelectron Spectroscopy Database, version 3.4 (web version), National Institute of Standards and Technology, Gaithersburg, MD, 2003 ⟨srdata.nist.gov/xps⟩.
[35] N. Fairley, CasaXPS, version 2.3.9, Casa Software Ltd., Teighnmouth, Devon, UK, 2003 ⟨www.casaxps.com⟩.
[36] C. Engemann, G. Kohring, A. Pantelouris, J. Hormes, S. Grimme, S.D. Peyerimhoff, J. Clade, F. Frick, M. Jansen, Chem. Phys. 221 (1997) 189–198.
[37] D.T. Jiang, E.D. Crozier, Can. J. Phys. 76 (1998) 621–643.

[38] B. Ravel, M. Newville, J. Synchrotron Rad. 12 (2005) 537–541.
[39] B. Aronsson, T. Lundström, S. Rundqvist, Borides, Silicides and Phosphides, Methuen, London, 1965.
[40] A.L. Allred, E.G. Rochow, J. Inorg. Nucl. Chem. 5 (1958) 264–268.
[41] A.P. Grosvenor, B.A. Kobe, M.C. Biesinger, N.S. McIntyre, Surf. Interface Anal. 36 (2004) 1564–1574.
[42] S. Oswald, H. Wirth, Surf. Interface Anal. 27 (1999) 136–141.
[43] R.G. Cavell, R.N.S. Sodhi, J. Electron Spectrosc. Relat. Phenom. 41 (1986) 25–35.
[44] R.N.S. Sodhi, R.G. Cavell, J. Electron Spectrosc. Relat. Phenom. 41 (1986) 1–24.
[45] K. Kotsis, V. Staemmler, Phys. Chem. Chem. Phys. 8 (2006) 1490–1498.
[46] N. Rössler, K. Kotsis, V. Staemmler, Phys. Chem. Chem. Phys. 8 (2006) 697–706.
[47] S. Doniach, M. Šunjić, J. Phys. C: Solid State Phys. 3 (1970) 285–291.
[48] S. Hüfner, in: L. Ley, M. Cardona (Eds.), Photoemission in Solids II, Springer, Berlin, 1979.
[49] R.F. Egerton, M. Malac, J. Electron Spectrosc. Relat. Phenom. 143 (2005) 43–50.
[50] H.A.E. Hagelin-Weaver, J.F. Weaver, G.B. Hoflund, G.N. Salaita, J. Alloys Compd. 389 (2005) 34–41.
[51] H.A.E. Hagelin-Weaver, G.B. Hoflund, D.M. Minahan, G.N. Salaita, Appl. Surf. Sci. 235 (2004) 420–448.
[52] A.P. Grosvenor, M.C. Biesinger, R.St-C. Smart, N.S. McIntyre, Surf. Sci. 600 (2006) 1771–1779.
[53] N. Moslemzadeh, G. Beamson, P. Tsakiropoulos, J.F. Watts, Surf. Sci. 600 (2006) 265–277.
[54] N. Moslemzadeh, G. Beamson, P. Tsakiropoulos, J.F. Watts, S.R. Haines, P. Weightman, J. Electron Spectrosc. Relat. Phenom. 152 (2006) 129–133.
[55] A.P. Grosvenor, R.G. Cavell, A. Mar, Phys. Rev. B. 74 (2006) 125102/1–125102/10.
[56] F.M.F. de Groot, S. Pizzini, A. Fontaine, K. Hämäläinen, C.C. Kao, J.B. Hastings, Phys. Rev. B 51 (1995) 1045–1050.
[57] F. de Groot, Coord. Chem. Rev. 249 (2005) 31–63.
[58] P.G. Perkins, A.K. Marwaha, J.J.P. Stewart, Theor. Chim. Acta 59 (1981) 569–583.
[59] T.E. Westre, P. Kennepohl, J.G. DeWitt, B. Hedman, K.O. Hodgson, E.I. Solomon, J. Am. Chem. Soc. 119 (1997) 6297–6314.